



# Molecular dynamics modeling of thermal resistance at argon-graphite and argon-silver interfaces

Ziyuan Shi, Murat Barisik, Ali Beskok\*

Old Dominion University, Institute of Micro and Nanotechnology, Mechanical & Aerospace Engineering Department, 4750 Elkhorn Ave, Rm 1300, Norfolk, VA 23529-0247, USA

## ARTICLE INFO

### Article history:

Received 5 December 2011

Received in revised form

9 April 2012

Accepted 10 April 2012

Available online 14 May 2012

### Keywords:

Kapitza resistance

Kapitza length

Nano-scale heat conduction

Temperature jump

## ABSTRACT

Heat conduction between two parallel solid walls separated by liquid argon is investigated using three-dimensional molecular dynamics (MD) simulations. Liquid argon molecules confined in silver and graphite nano-channels are examined separately. Heat flux and temperature distribution within the nano-channels are calculated by maintaining a fixed temperature difference between the two solid surfaces. Temperature profiles are linear sufficiently away from the walls, and heat transfer in liquid argon obeys the Fourier law. Temperature jump due to the interface thermal resistance (i.e., Kapitza length) is characterized as a function of the wall temperature. MD results enabled development of a phenomenological model for the Kapitza length, which is utilized as the coefficient of a Navier-type temperature jump boundary condition using continuum heat conduction equation. Analytical solution of this model results in successful predictions of temperature distribution in liquid argon confined in silver and graphite nano-channels as thin as 7 nm and 3.57 nm, respectively.

© 2012 Elsevier Masson SAS. All rights reserved.

## 1. Introduction

Thermal resistance at the solid–fluid interface has great importance in thermal/fluid engineering. Low thermal interface resistance enables efficient heat dissipation and consistent device performance in microelectronic semiconductor devices [1]; and permits enhanced thermal transport properties of nanofluids (i.e., coolants seeded with conductive nano-particles) [2,3]. On the other hand, high interface resistance is useful for thermal isolation of device components.

Thermal transport through an interface between two dissimilar materials results in a temperature jump ( $\Delta T$ ). For a given heat flux ( $\vec{j}$ ), this jump can be identified as a thermal resistance ( $R_K$ ), written as

$$\Delta T = -R_K \vec{j} \cdot \vec{n}, \quad (1)$$

where  $\vec{n}$  is the outward unit normal from the wall. The interface resistance was discovered by Kapitza in 1941 on a metal–liquid interface, and hence, known as the Kapitza resistance [4]. One can define a thermal resistance length ( $L_K$ ), known as the Kapitza length, by extrapolating the temperature profile from liquid in to

the solid, where the wall temperature is reached. The Kapitza length can be predicted using

$$\Delta T = L_K \left. \frac{\partial T}{\partial n} \right|_{\text{liquid}} \quad (2)$$

where  $\partial T/\partial n$  is the thermal gradient on the liquid side, and  $\Delta T = T_{\text{fluid}} - T_{\text{wall}}$ . It is crucial to realize that Eq. (2) requires onset of continuum behavior where a local temperature profile can be defined, and it can be used as a Navier-type boundary condition in solution of continuum based heat transfer equations. Eqs. (1) and (2) can be manipulated to relate the Kapitza resistance ( $R_K$ ) and Kapitza length ( $L_K$ ) using the Fourier law.

There are several continuum based interface thermal resistance models. For instance, the Acoustic Mismatch Model (AMM) explains thermal resistance at the liquid/solid interface using the impedance of phonon energy transfer across the interface [4]. Phonon radiation and acoustic impedance are the two determining factors of thermal resistance in AMM, which neglects phonon scattering at the interface. The Diffuse Mismatch Model considers diffuse scattering of phonons on the interface, followed by their emission into the neighboring material with a probability proportional to the phonon density of states within the respective materials. This model determines the interface thermal resistance by utilizing the mismatch between the phonon density of states within two materials [5]. Recently developed Scattering Mediated Acoustic Mismatch Model

\* Corresponding author. Tel.: +1 757 683 6818.

E-mail address: [abeskok@odu.edu](mailto:abeskok@odu.edu) (A. Beskok).

Nomenclature		Greek symbols	
<i>English symbols</i>		$\alpha(T_w)$	Wall temperature coefficient, nm
$e_i$	Energy per-atom, J	$\varepsilon$	Depth of potential well, eV
$f_{ij}$	Force acting on molecule i from molecule j, N	$\varepsilon_{wf}$	Liquid–solid interaction strength, eV
$\vec{j}$	Heat flux, mW/m <sup>2</sup>	$\Delta T$	Temperature jump, K
$H$	Channel height, nm	$\rho$	Number density, #
$L_K$	Kapitza length, nm	$\sigma$	Molecular diameter, nm
$m$	Mass, kg	$\Omega$	Volume, nm <sup>3</sup>
$\vec{n}$	Unit normal vector	$\omega_f$	Thermal oscillation frequency of fluid
$r_{ij}$	Spacing between the molecules i and j, nm	$\omega_w$	Thermal oscillation frequency of wall
$R_K$	Thermal resistance, mW/mK	<i>Subscripts</i>	
$T$	Temperature, K	i	Molecule i
$\partial T/\partial n$	Thermal gradient, K/nm	j	Molecule j
$x$	Direction normal to surface, nm	f	Fluid
$v_i$	Velocity, m/s	l	Liquid
		Low	Low temperature reservoir
		High	High temperature reservoir
		w	Wall

describes phonon transport via a damped wave equation using an analogy between phonon and radiative energy transport [6]. Despite these theoretical developments, predictions of these models are only accurate at extremely low temperatures.

Alternative to the continuum based studies; interface resistance between two dissimilar materials can be investigated using molecular dynamics (MD), which does not require continuum based governing equations and constitutive laws. There are several MD studies on interface thermal resistance between solids and liquids, but most of these had limited success in explaining and quantifying the Kapitza length. The earliest work was by Maiti et al., who reported a temperature jump at the solid–liquid interface [7]. Several research groups investigated the relationship between the interface thermal resistance and wettability, and have shown decreased resistance with increased solid/liquid interaction strength [8]. Structural changes in the interfaces also affect the interface resistance [9]. Torii et al. showed that the energy transfer in directions parallel to the interface are governed by surface corrugations at the molecular-scale, and energy transfer in the direction perpendicular to the surface is governed by the molecular number density on solid surfaces [10]. More recently, Liu et al. investigated flow dependence of the interface thermal resistance of argon in copper and silver channels, and found “solid like” behavior of argon near the walls [11]. These authors reported increased thermal resistance due to adsorption of argon on the walls.

In order to investigate thermal transport in nano-scale confined “simple liquids” like argon, Kim et al. utilized a thermal wall model that considered each wall molecule as an independent oscillator with a given crystal bonding stiffness [12]. Their model applied a thermostat on the walls to maintain channel walls at desired temperatures, while the fluid domain was free of thermostat to enable MD simulations of liquid flow and heat transfer. In a following study, same authors investigated interface thermal resistance and proposed a Navier-type temperature jump boundary condition, which predicted temperature profiles in nano-channels using continuum heat conduction equation [13]. By hypothesizing that the temperature jump  $\Delta T = f(\omega_w/\omega_f, \varepsilon_{wf}/\varepsilon, T_w, \partial T/\partial n)$ ,

$$\Delta T = \alpha(T_w) \left( \frac{\omega_{wall}}{\omega_{fluid}} \right)^4 \exp\left(-1.85\varepsilon_{wf}/\varepsilon\right) \frac{\partial T}{\partial n} \Big|_{liquid'} \quad (3)$$

where  $\alpha(T_w)$  is a coefficient with the unit of length-scale dependent on the wall temperature,  $\omega_w/\omega_f$  is the relative thermal oscillation frequency of wall and liquid,  $\varepsilon_{wf}/\varepsilon$  is the liquid–solid interaction

strength, and  $\partial T/\partial n$  is the thermal gradient on the liquid side, respectively. Performing systematic simulations by varying the nano-channel dimensions, they verified onset of thermal equilibrium and Fourier law for liquid argon in nano-channels as small as 3.24 nm. While the Eq. (3) is related to the Kapitza length via Eq. (2), the authors characterized the Kapitza length ( $L_K$ ) as a function of the relative thermal oscillation frequencies of the liquid–solid pair, liquid–solid interaction strength, and wall temperature [13]. In a subsequent study, the same temperature jump model was validated for viscous heating in linear Couette flow within nano-channels [14]. The primary drawbacks of their studies were that wall molecules had similar mass and radius with liquid argon, and each wall molecule exhibited simple harmonic vibrations with a single degree of freedom. In reality, the vibration of wall molecules is often more complex and exhibit multiple degrees of freedom. Hence, direct application of their model to realistic surfaces like silver or graphite is limited.

In this paper, we investigate heat conduction between two parallel solid walls separated by liquid argon via three-dimensional molecular dynamics simulations using LAMMPS 2010 [15]. Instead of defining  $L_K$  based on the molecular level details of representative surfaces, we investigate its variation on real surfaces simply as a function of wall temperature. The *objectives* of this study are (1) determination of the Kapitza length for the argon–silver and argon–graphite interfaces as a function of the local wall temperature; (2) development of a phenomenological model for the Kapitza length for these interfaces; (3) and verification of this new model by comparisons of MD results with the predictions of continuum heat conduction equation subjected to the temperature jump boundary conditions in various size nano-channels.

This paper is organized as follows: In section 2, we summarize the MD simulation details which include a description of the simulation domain, heat flux calculation and summary of the simulation parameters. Section 3 contains investigation of heat conduction in nano-channels and determination of the Kapitza length at liquid argon/silver, and argon/graphite interfaces. This is followed by introduction of a Navier boundary condition which is verified using MD simulation results. Finally, conclusions are presented.

## 2. Molecular dynamics simulation details

The simulation domain, schematically shown in Fig. 1, consists of two parallel solid walls and liquid argon molecules between

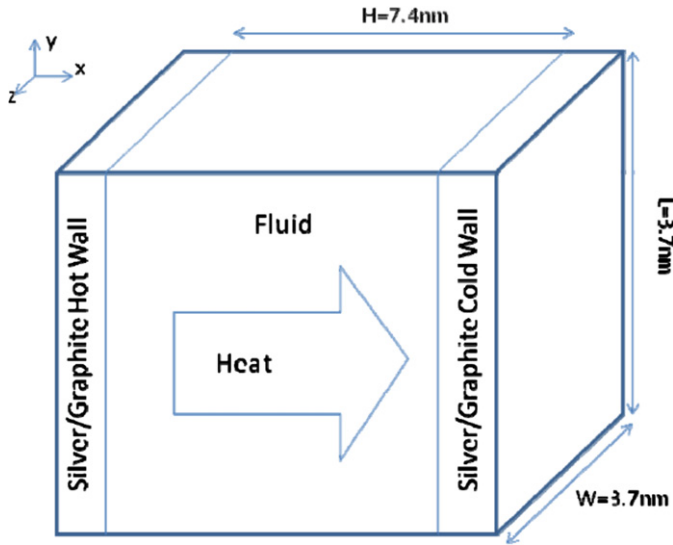


Fig. 1. Schematics of the computational domain.

them. We simulated three-dimensional nano-channels of 7.4 nm and 7.6 nm in height for silver and graphite channels, respectively. The channels' widths and lengths are 3.7 nm for all cases. Periodic boundary conditions were applied in the  $y$ - and  $z$ -directions for both solid and liquid domains. Silver walls were modeled as face-centered cubic (FCC) structures with (0, 0, 1) crystal plane facing the fluid. By considering approximately 1 nm force cutoff distance for argon, four layers of silver atoms were used to model the silver channel. Three layers of graphite walls were modeled. Each layer of graphite had planar structure and the carbon atoms were arranged in a hexagonal lattice with separation of 0.142 nm, and the distance between the graphite layers was 0.335 nm. Atoms in the outmost layers of silver and graphite surfaces were fixed to maintain a stable system, while the atoms in other layers were free to move. A total of 2068 argon molecules were simulated in the three-dimensional channel, and the corresponding number density ( $N\sigma^3/\Omega$ ) of the system was set at  $\rho = 0.8$ , where the mass for an argon molecule was  $m = 6.63 \times 10^{-26}$  kg, and its molecular diameter was  $\sigma = 0.3405$  nm. We used the Lennard–Jones (12–6) potential for interaction of argon molecules, and the depth of the potential well ( $\epsilon$ ) for argon was 0.0103 eV. Silver wall–wall interactions were modeled using *embedded atom method* (EAM) since it can give an accurate description for the total energy of a metal by calculating the embedding energy as a function of the atomic electron density. EAM is a many-body potential and works especially well for FCC metallic structures [16]. In order to simulate the intramolecular forces of the graphite slabs, *Adaptive Intermolecular Reactive Empirical Bond Order* (AIREBO) potential is employed for the graphite wall–wall interactions. The AIREBO potential consists of three terms. First term is the REBO hydrocarbon potential describing short-ranged carbon–carbon interactions ( $r < 2\text{\AA}$ ). These interactions have strong coordination-dependence through a bond order parameter, which adjusts the attraction between atom couples based on the position of other nearby atoms, and thus has third- and fourth-body dependence. Second term is the Lennard–Jones (12–6) potential which adds longer-ranged interactions ( $2\text{\AA} < r < \text{cutoff}$ ). It contains a series of switching functions so that the short-ranged LJ repulsion ( $1/r^{12}$ ) does not interfere with the potential captured by the REBO term. The TORSION is the third term which is an explicit 4-body potential to describe various dihedral angle preferences in carbon configurations. The AIREBO potential is widely used for calculating the potential energy of covalent bonds and the inter-atomic forces [17]. The wall

parameters are shown in Table 1. Fluid-wall interactions were calculated using the Lennard–Jones potential. The Lorentz–Berthelot mixing rule was employed to calculate the Lennard–Jones parameters for fluid–wall interactions [18]. MD parameters utilized for Ar–Ar, Ar–Ag and Ar–C interactions are shown in Table 2.

Initially we applied NVT ensemble to the entire system to establish an equilibrium state, Nose–Hoover thermostat was applied to the molecules to maintain the system's temperature at 100 K. In order to induce a heat flux through the solid/liquid interfaces, different wall temperatures were assigned and maintained using Langevin thermostat, while NVE ensemble was applied to the liquid argon domain. Therefore, solid surfaces serving as heat baths were assumed to have infinite conductivity, and the effects of heat conduction on solid surfaces were neglected. The simulation time step was 4 fs for silver walls and 1 fs for graphite walls. Heat transfer simulations were performed for 10 ns, 2 ns for the system to reach steady-state and another 8 ns for averaging.

The thermal gradient applied in the simulation system generates a constant heat flux  $\vec{j}$ , calculated as [19]

$$\vec{j} = \frac{1}{\Omega} \left( \sum_i e_i v_i + \sum_{i<j} (f_{ij} \cdot v_j) r_{ij} \right), \quad (4)$$

where  $\Omega$  is the volume of the system,  $e_i$  is energy per-atom (potential and kinetic),  $v_i$  is the velocity of molecule  $i$ ,  $f_{ij}$  is the force acting on molecule  $i$  from molecule  $j$ , and  $r_{ij}$  is the distance between the molecules  $i$  and  $j$ . Before we present the temperature profiles and discuss how to calculate the thermal conductivity, it is necessary to demonstrate local thermal equilibrium in the system. Local temperature can be defined only if the local thermal equilibrium is established. Kim et al., [13], calculated the normal distribution of molecular velocity in an equilibrium system, and showed that the skewness and kurtosis for randomly selected bins varied between  $-0.097$  and  $0.054$  and  $-0.092$  to  $0.202$ , respectively. As a result, they claimed onset of local thermal equilibrium. In this paper, temperature distribution is obtained using both 20 and 200 slab bins parallel to the walls. For the coarse bin case, each slab bin contains more than 30 atoms, NVE ensemble of these atoms for 8 ns is adequate to achieve local thermal equilibrium, in which, the velocity distribution of atoms follows the Maxwell–Boltzmann distribution [20]. We also calculated the skewness and kurtosis of select bins in the channel center and next to the walls, and have observed their values varying between  $-0.056$  and  $0.063$  and  $-0.049$  to  $0.087$ , respectively. In order to interpret the temperature profiles obtained using fine-bins, we plot and compare the temperature distribution obtained using 20 and 200 slab bins. Temperature profiles from the fine and coarse bins cases are consistent, and show that local thermal equilibrium is reached. In all our analysis, wall positions are defined at the center of the first layer of wall molecules adjacent to the fluid.

### 3. Results

In this section we first show the density and temperature profiles obtained in liquid argon in contact with silver and graphite

Table 1  
Molecular parameters used for solid walls.

Wall	$\sigma$ (Å)	$\epsilon$ (eV)	Mass (g/mol)	Lattice constant (Å)	Number of molecules for each wall	Number of wall layers
Ag	2.551	0.408	107.9	4.086	648	4
Carbon	3.4	0.003	12	N/A	490/504	3

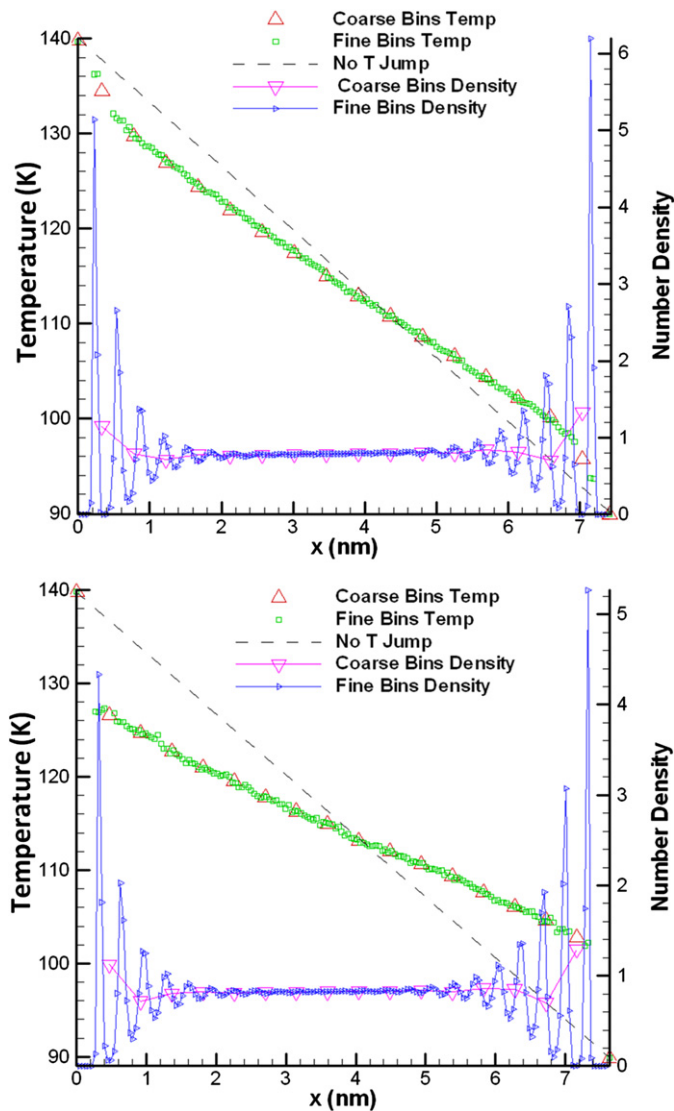
**Table 2**  
Intermolecular interaction parameters used in the simulations.

Interaction	$\sigma$ (Å)	$\epsilon$ (eV)	$\epsilon/\epsilon_{\text{Ar}}$
Ar–Ar	3.405	0.01	1
Ar–Ag	2.978	0.06	6
Ar–C	3.403	0.005	0.5

walls subjected to different wall temperatures. Then we utilize MD results to develop a phenomenological model for the Kapitza length, and verify this model by comparisons of the continuum heat conduction equation solutions with MD results obtained for different channel dimensions and temperatures.

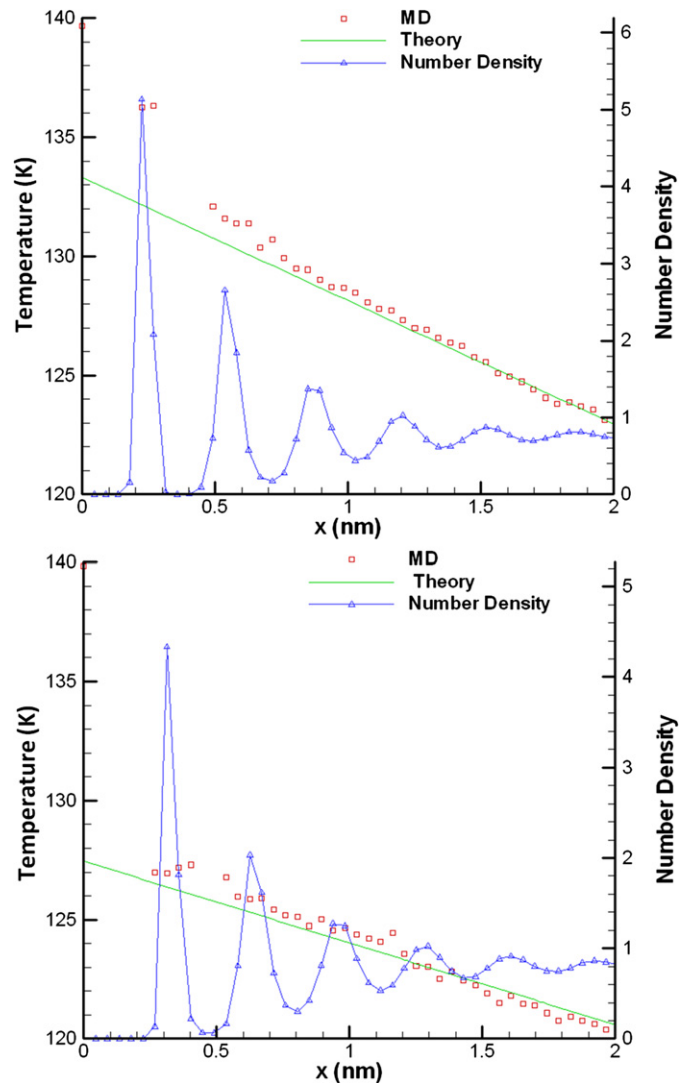
### 3.1. Liquid argon in silver and graphite nano-channels

Fig. 2 shows the number density (normalized by the molecular diameter of argon  $\sigma^3$ ) profiles obtained for liquid argon facing silver and graphite surfaces subjected to 140 K and 90 K on their left and right surfaces, respectively. In order to capture the density layering phenomenon, we divided the whole domain into 200 (fine) slab



**Fig. 2.** Density distribution and temperature profile of liquid argon facing silver (top) and graphite (bottom) surfaces. Left and right surfaces of each channel are subjected to 140 K and 90 K, respectively. Temperature and density profiles obtained using 20 and 200 slab bins are shown.

bins. Results obtained using 20 (coarse) slab bins are also shown in the figure. Driven by the wall force field effects and local argon–argon interactions, the density profile exhibits strong near wall layering that extends approximately 2 nm from each surface. Asymmetry in the density profiles shows the effects of wall temperature on density for each case. Local argon density near high temperature walls is less than the argon density near low temperature walls for both silver and graphite surfaces. Differences in the density profiles as a function of the wall type can be correlated with the argon–silver and argon–graphite interaction properties given in Table 2. Specifically, the interaction potential ratio of argon–silver to argon–argon molecules is  $\epsilon_{\text{Ar–Ag}}/\epsilon_{\text{Ar}} = 6$ , while this value for the argon–graphite pair is  $\epsilon_{\text{Ar–C}}/\epsilon_{\text{Ar}} = 0.5$ . As a result, the interactions of argon molecules with silver walls are twelve times stronger than the interactions of argon with graphite surfaces. This creates a larger near wall argon density peak in silver nano-channels than the graphite channels. For both surfaces, liquid argon density fluctuates severely near the surface, resulting in nearly zero molecules within certain bins. A zoomed view of the density and temperature profiles within 2 nm from the walls are shown in Fig. 3. The first and second liquid argon density maxima is 0.223 nm and 0.536 nm away from the silver channel kept at 140 K, while the locations of these maxima



**Fig. 3.** Density and temperature profiles of liquid argon within 2 nm distance of silver (top) and graphite (bottom) surfaces kept at 140 K. Theoretical predictions correspond to the phenomenological model developed in this work.

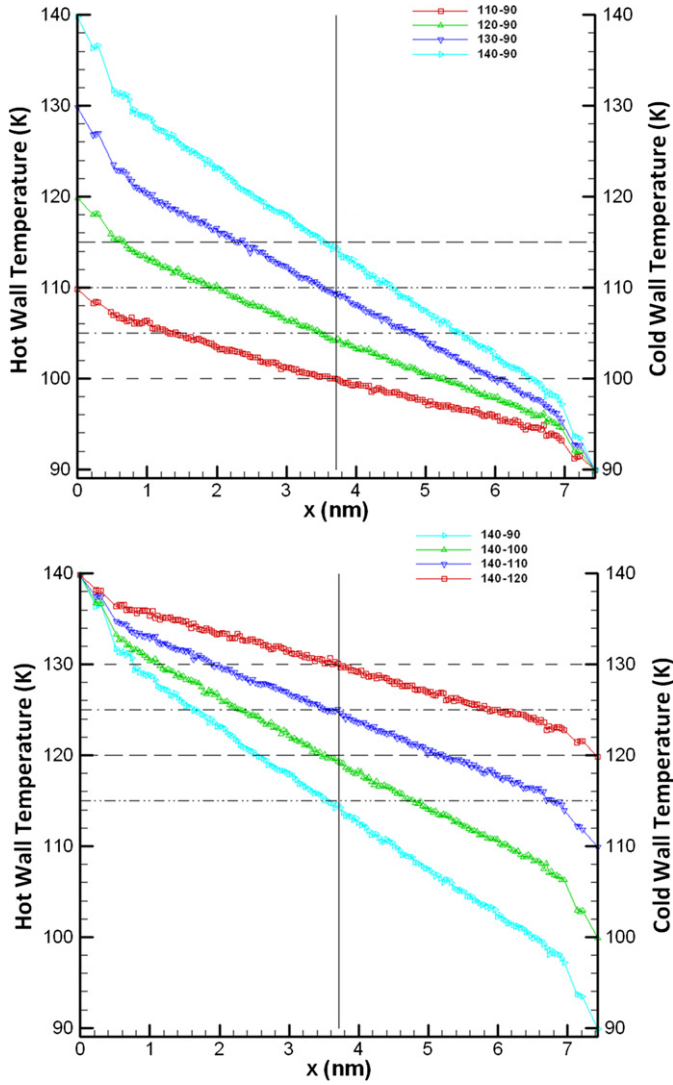


Fig. 4. Temperature profiles for argon in silver nano-channels subjected to various wall temperatures.

are 0.313 nm and 0.625 nm away from the graphite wall. Since the attraction between argon and graphite molecules is much smaller than the argon-silver pair, there are more “empty” bins in between the first argon layer and graphite walls. Depletion of argon molecules near the surfaces has profound effects on the definition of local liquid temperature. Very few liquid molecules are present at these density minima, and hence, one cannot define the local temperature accurately. In order to address this problem we omitted presentation of temperature in these “empty” bins as can be deduced from the near wall temperature profiles.

Fig. 2 also shows the temperature profiles within the entire domain obtained using 20 and 200 slab bins. The left surface is kept at 140 K, while the right surface is kept at 90 K. Liquid argon temperature varies linearly in bulk of the nano-channel. Temperature jumps at the liquid/solid interfaces are apparent in the results. The temperature profiles obtained using 20 and 200 slab bins gave very similar results in the bulk of the channel, validating thermal equilibrium for both fine and coarse bin cases. Extrapolations of the liquid temperature on to the walls reveal discontinuities between the extrapolated fluid temperature and wall temperature. These temperature jumps are related to the Kapitza resistance and the Kapitza length, as can be deduced from Eqs. (1) and (2). Fig. 2 shows drastic differences in temperature profiles for

the graphite and silver cases. Therefore, these simulations exhibit different heat flux values. In order to characterize the temperature distribution in the bulk of the channels, we performed linear least square fits to the MD data and measured  $r^2$ , which is the measurement of how well the least square fit represents the data. The values are all above 99%, which means that the temperature profile is linear in the bulk of the channel. Linear fits to the temperature profiles are shown in Fig. 3 as the theoretical fits, which also correspond to the predictions of the phenomenological models that will be developed in the next section. Surprisingly, linear temperature profiles are observed up to the second argon density peak, approximately 0.536 nm from the silver wall, while linear temperature profile is observed 0.313 nm from the graphite surface. Hence, strong density fluctuations shown in Figs. 2 and 3 do not significantly affect the temperature profile beyond 0.313 nm and 0.536 nm from the graphite and silver surfaces, respectively. In addition, the fine bin temperature distribution in liquid argon near the silver surface, especially within the first density peak near the walls, shows steep temperature variations compared to the bulk region. This behavior was not observed in the graphite channel cases, despite equivalently large density fluctuations of liquid argon near graphite walls. Differences in this

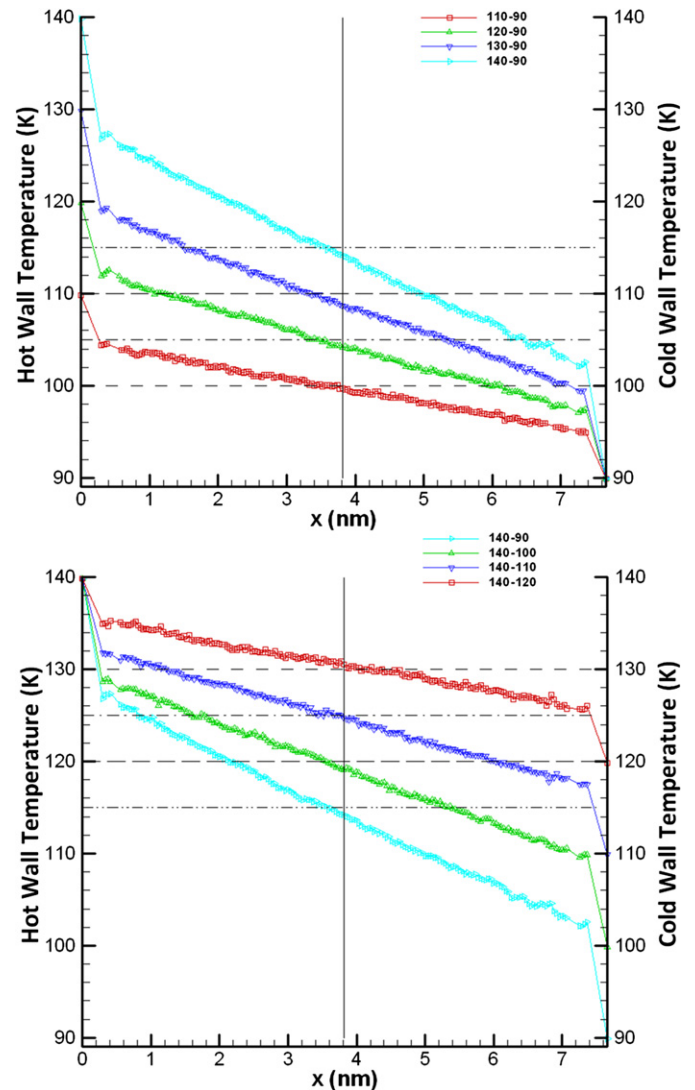


Fig. 5. Temperature profiles for argon in graphite nano-channels subjected to various wall temperatures.

**Table 3**  
Thermal conductivity for liquid argon at 100 K.

Average temperature (K)	Thermal conductivity in this work (mW/mK)	Thermal conductivity from previous MD results (mW/mK)	Thermal conductivity from experimental results (mW/mK)
100	108.92	101.24 [13] 110.00 [22] 102.70 [25]	108.71 [23] 112.60 [26] 104.18 [27]

behavior can be attributed to twelve folds stronger interactions between the silver-argon molecules than the argon-graphite pair.

### 3.2. Determination of the Kapitza length

In previous MD studies, the Kapitza length was shown to be a function of the wall temperature [13,21]. In order to investigate

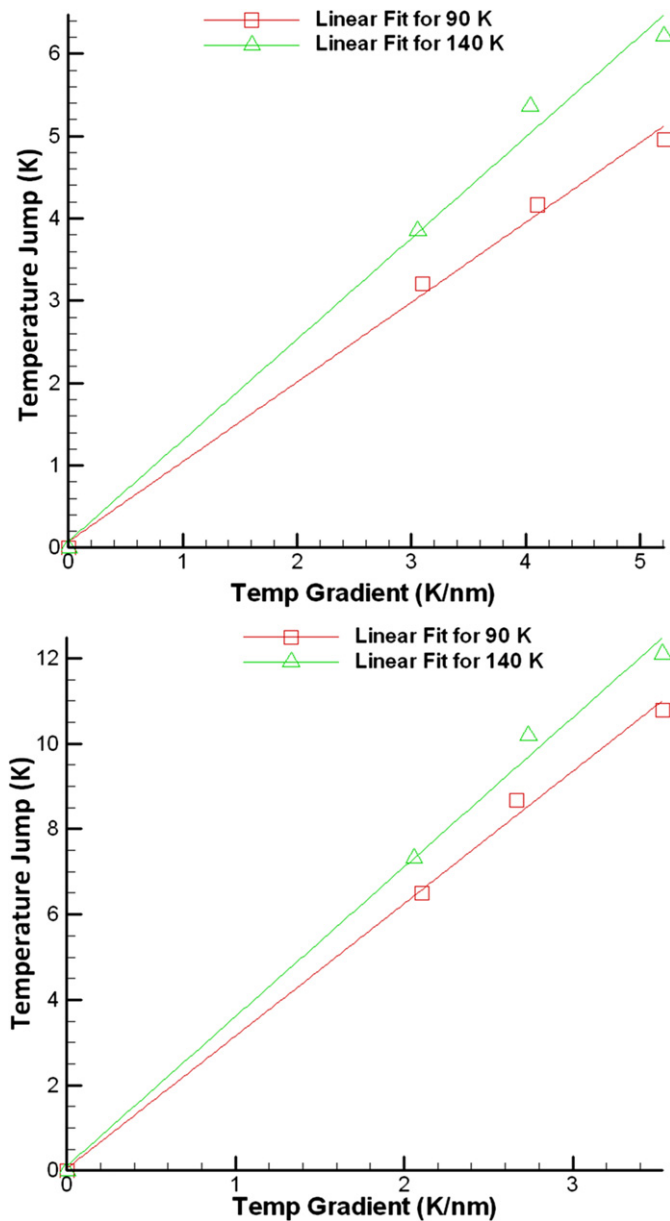


**Fig. 6.** Temperature jump versus the temperature gradient at argon-silver (top) and argon-graphite (bottom) interfaces kept at 90 K and 140 K. Lines show the least square fit to data, while the Kapitza length,  $L_K$ , is given by the slope of these lines.

the effect of wall temperature on the Kapitza length, we performed a series of MD simulations for liquid argon in silver and graphite channels. We first fixed the right wall temperature at 90 K and gradually increased the left wall temperature up to 140 K. Then we fixed the left wall temperature at 140 K and gradually decreased the right wall temperature to 90 K. These simulations result in different heat flux values and temperature gradients. Figs. 4 and 5 show the temperature profiles for liquid argon in silver and graphite nano-channels, respectively. The figures also show the channel center line and the average temperature of liquid argon so that one can visually assess the breakdown of rotational symmetry in temperature profiles. We observe a systematic undershoot between the liquid temperature at the channel center line and the average temperature in the system. This effect is more dominant for the cases with large temperature gradients. Lack of rotational symmetry in the temperature profiles shows temperature dependence of the Kapitza length for both interfaces.

In order to investigate the temperature dependence of the Kapitza length quantitatively, we calculated the Kapitza length for each case by using Eq. (2). First we obtained the local temperature gradients from MD results, and matched these with the slope of the

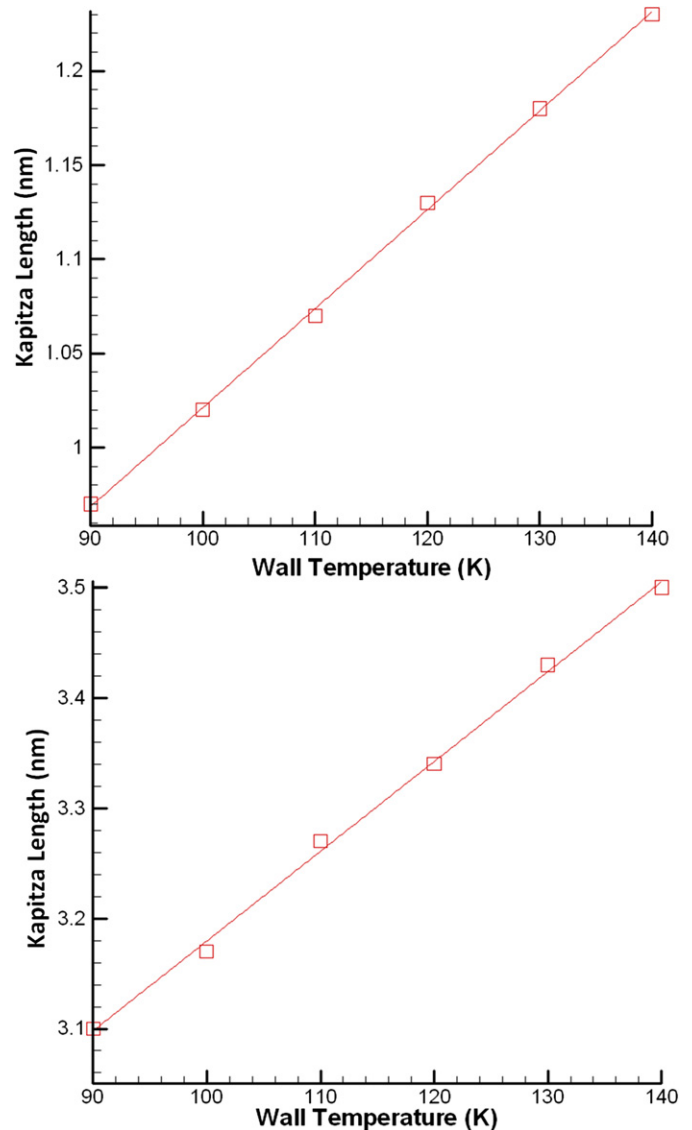


**Fig. 7.** Variation of the Kapitza length as a function of the wall temperature for silver-argon (top) and graphite-argon (bottom) cases. Lines show the least square fit to data.

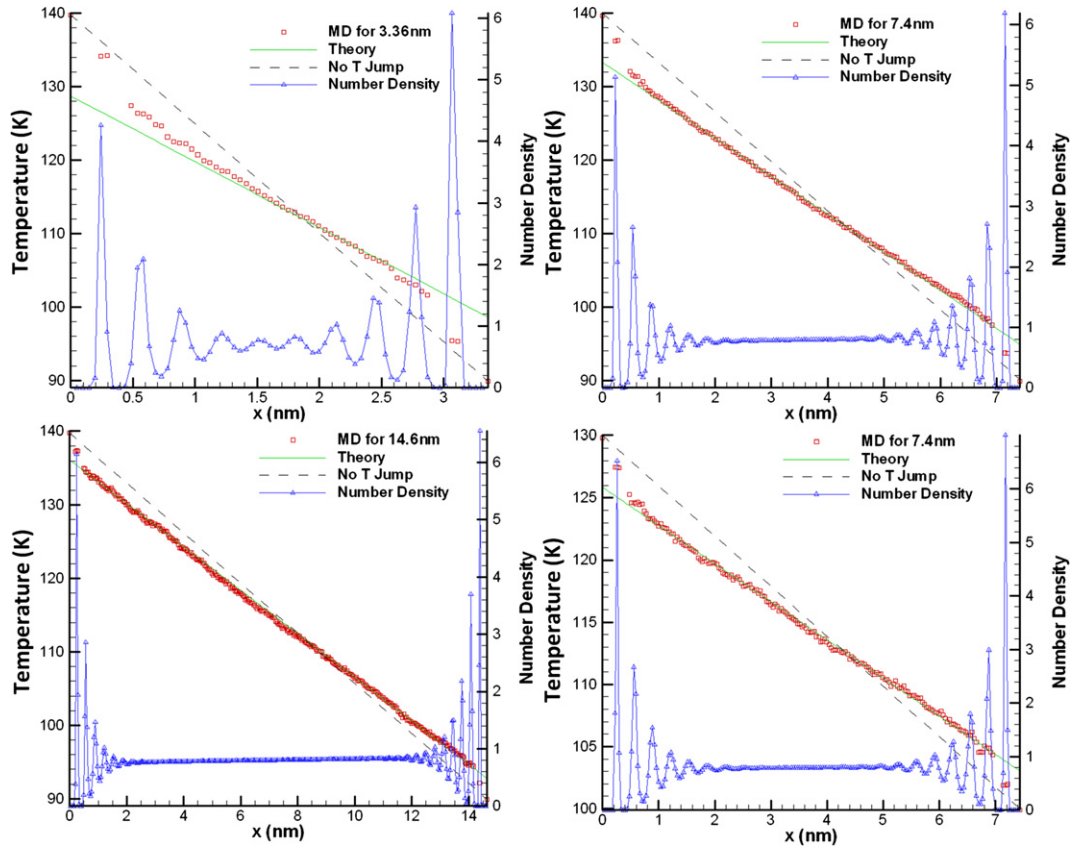


Fig. 8. Temperature and number density distributions of liquid argon in various silver nano-channels. MD results are compared with continuum solutions subjected to a temperature jump based on the MD predicted Kapitza length. Continuum solution with zero temperature jump is also shown.

linear curve fits to the temperature profiles in the bulk of the channel. Extrapolation of the temperature profile onto the solid surface enabled us to calculate the local temperature jump ( $\Delta T = T_{\text{fluid}} - T_{\text{wall}}$ ), which yielded a value for  $L_K$  using Eq. (2). In the mean time, we also calculated heat flux values using Eq. (4), and utilized the temperature gradient from MD results to calculate the thermal conductivity using Fourier law. As can be seen in Table 3, thermal conductivity for liquid argon at average temperature of 100 K is 108.92 mW/mK, which matches the published bulk values well [22,23]. In order to show the relationship of the Kapitza length and wall temperature visibly, we present the variation of temperature jump as a function of the temperature gradient for silver and graphite walls kept at 90 K and 140 K in Fig. 6. The lines naturally pass from the origin, since liquid in thermal equilibrium will not experience any heat transfer, and therefore, no temperature jumps are expected. Slopes of these lines result in the Kapitza length, as can be deduced from Eq. (2). Least square fit to the data gives  $L_K$  (90 K) = 0.97 nm and  $L_K$  (140 K) = 1.23 nm for liquid argon in contact with silver walls, while we obtained  $L_K$  (90 K) = 3.1 nm and  $L_K$  (140 K) = 3.5 nm for liquid argon in contact with graphite walls. These results clearly indicate the temperature dependence of Kapitza length for argon-silver and argon-graphite interfaces.

In order to further examine the temperature dependence of Kapitza length, we repeated the procedure shown in Fig. 6 for silver and graphite walls kept at 100 K, 110 K, 120 K, and 130 K. Fig. 7 shows variation of the Kapitza length as a function of the wall temperature. Within the 90 K–140 K range, Kapitza length for the argon-silver and argon-graphite interfaces increases linearly with the surface temperature. Using linear fits to data in Fig. 7, we obtained  $L_K(T_w) = 0.0052T_w + 0.502$  for argon-silver, and  $L_K$

( $T_w$ ) =  $0.008T_w + 2.38$  for argon-graphite interfaces. Thermal slip length for the argon-graphite interface is approximately three times larger than that of the argon-silver interface. Differences in the Kapitza lengths are due to the differences in the atomistic properties and structures of these surfaces (see Tables 1 & 2, and section 2).

### 3.3. Model verification

To this point, we developed phenomenological models for the thermal slip length between liquid argon and various surfaces using extensive MD simulations. In this section, we utilize these slip lengths within a Navier-type temperature jump boundary condition given by Eq. (2). Specifically, the temperature jump at the argon-silver interface is modeled by

$$\Delta T = (0.0052T_w + 0.502) \left. \frac{\partial T}{\partial n} \right|_{\text{liquid}} \quad (5)$$

while the temperature jump boundary condition for the argon-graphite interface is given by

$$\Delta T = (0.008T_w + 2.38) \left. \frac{\partial T}{\partial n} \right|_{\text{liquid}} \quad (6)$$

These temperature jump models include only the macroscopic thermal conditions such as the thermal gradient and wall temperature, and developed using MD simulation data. Utilizing these jump conditions in the solution of heat conduction equation as boundary conditions result in the following analytical solution for the temperature distribution

$$T(x) = \left( \frac{T_{\text{Low}} - T_{\text{High}}}{L_{K-\text{High}} + L_{K-\text{Low}} + H} \right) (x + L_{K-\text{High}}) + T_{\text{High}} \quad (7)$$

where  $T_{\text{Low}}$  and  $T_{\text{High}}$  correspond to the specified wall temperatures,  $H$  is the channel Height, and the Kapitza length  $L_K$  is determined as a function of the local wall temperature. In the following we present verification of the continuum model given by Eq. (7) for liquid argon in different height silver and graphite nano-channels subjected to various temperature differences. These test cases are chosen specifically outside the model development range, so that sensitivity of this continuum based model to the nano-channel length-scale and thermal gradients can be tested. In MD simulations, the nano-channel height is varied from 3.36 nm to 14.9 nm, while keeping other dimensions of the channels unchanged. In Figs. 8 and 9 the number density and temperature profiles are plotted together to demonstrate the influence of density layering on temperature distribution. Predictions of the heat conduction equation subjected to zero-jump and temperature jump based on Eqs. (5) and (6) are also shown to validate the extent of the continuum model.

Fig. 8 shows the temperature and density profiles of liquid argon confined in silver nano-channels of 3.36, 7.4 and 14.6 nm in height, and subjected to 140 K and 90 K from side walls (top-left, top-right and bottom-left figures, respectively). Result for 7.4 nm channel subjected to 130 K and 100 K on its walls is also shown on the bottom-right figure. In silver channels with dimensions larger than 3.36 nm, density layering effects the temperature distribution

mostly in the first two density peak regions near the walls, and the temperature profile becomes almost linear starting from the third density peaks from each wall. Strong interactions between silver and argon molecules ( $\epsilon_{\text{Ar-Ag}}/\epsilon_{\text{Ar}} = 6$ ) affect heat transfer in the near wall region, and results in distinct temperature variations from the bulk section. Therefore the analytical model in Eq. (7) is valid beyond the near wall region that extends approximately 0.536 nm from each silver surface. MD results in the 3.36 nm high silver channel (Fig. 8 top-left) exhibit further deviations from the continuum model predictions. The reason for this is the small dimensions of the channel. The wall force field penetrates 1 nm from each wall, and the density layering penetrates approximately 2.0 nm from each surface. Therefore density layering effects in 3.36 nm high silver channel overlaps from both walls, inducing further deviations from the continuum model.

Fig. 9 shows the temperature and density profiles for liquid argon confined in graphite channels of 3.57, 7.6 and 14.9 nm in height, and subjected to the identical wall temperatures in Fig. 8. Temperature profiles in various sized nano-channels are linear in the bulk and near wall regions, and the continuum model given by Eq. (7) is equivalently valid in different sized nano-channels, including the 3.57 nm channel. Near wall effects apparent in silver channels are not as strong in the graphite channels, which is due to the relatively lower interaction strength ratios between argon and carbon molecules ( $\epsilon_{\text{Ar-C}}/\epsilon_{\text{Ar}} = 0.5$ ). From Figs. 8 and 9, we can observe excellent matches between the continuum predictions and analytical solution for the silver and graphite cases in channels larger than 7 nm and 3.57 nm, respectively.

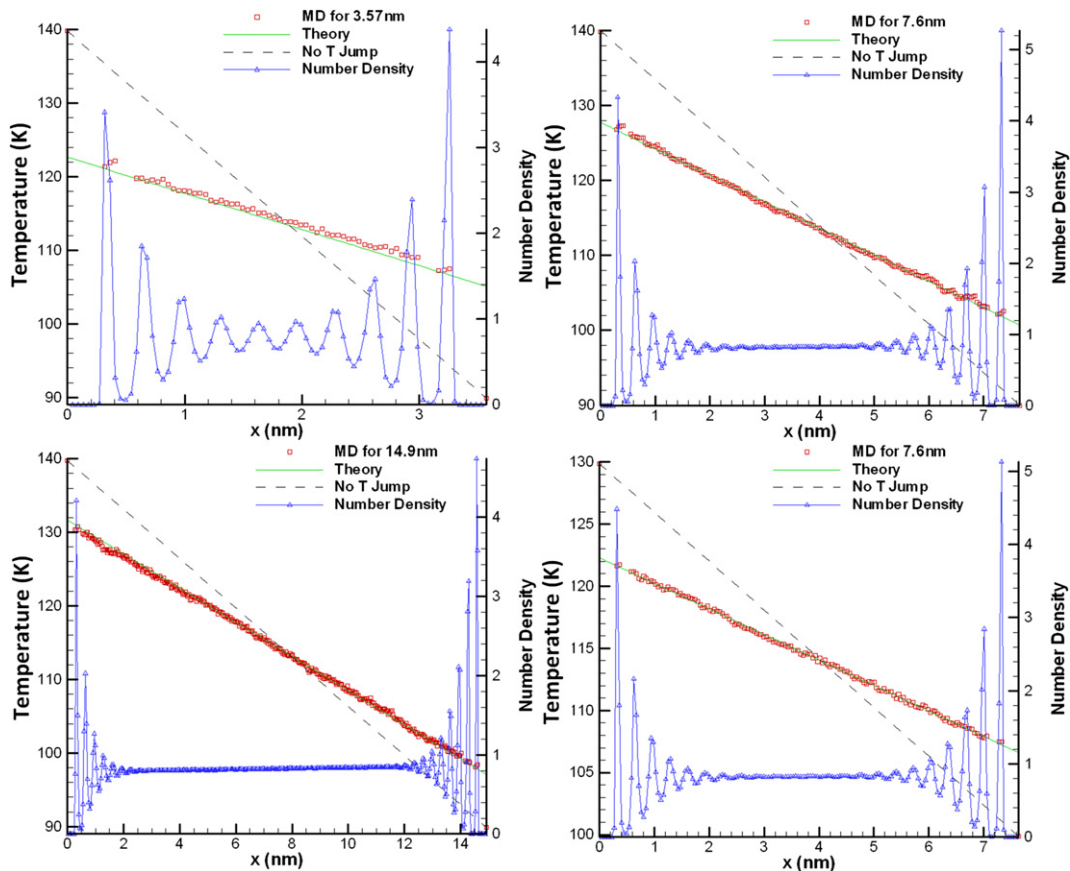


Fig. 9. Temperature and number density distributions of liquid argon in various graphite nano-channels. MD results are compared with continuum solutions subjected to a temperature jump based on the MD predicted Kapitza length. Continuum solution with zero temperature jump is also shown.

#### 4. Conclusions

In this paper, we utilized MD simulations to perform systematic studies of thermal transport in liquid argon confined within nano-channels and thermal resistance at the argon/solid interfaces. The current study was limited to liquid argon, which was modeled using 12–6 Lennard–Jones interaction potential. Channel walls were modeled as FCC silver, and graphite surfaces. Wall–wall interactions were modeled using the EAM and AIREBO potentials for silver and graphite walls, respectively; with no electrical charges or long-range force fields. Density profiles of liquid argon exhibited well known layering near the solid surfaces. The peak density values are shown to increase with decreased wall temperature. Temperature profiles consistently exhibited jumps at the liquid/solid interfaces due to the interface thermal resistance. Assuming isothermal walls induced by a thermostat, we performed systematic studies of the Kapitza length as a function of the wall temperature, and consistently observed larger Kapitza length on higher temperature surfaces, which agreed with previous MD studies in [13]. Kapitza length at the argon–silver interface is approximately three times smaller than that at the argon–graphite interface. This is due to the twelve times difference between the interaction potential of argon–silver and argon–carbon molecular pairs. Our results are consistent with the literature [8,13,24], and show decreased Kapitza length and interface resistance with increased interaction strength between solids and liquids.

Using MD results, we developed phenomenological models for  $L_K$  as a function of the wall temperature for silver and graphite surfaces. Utilizing these within the temperature jump boundary condition enabled us to predict the temperature distribution in nano-channels using continuum based models. The resulting temperature profiles were shown to agree with MD predictions at arbitrary wall temperature values and channel heights as small as 7 nm and 3.57 nm for silver and graphite walls, respectively. Investigation of more complex surfaces, effects of electrical charges and polar fluids will be the topic of future research.

#### Acknowledgment

This work was supported by the National Science Foundation under Grant No: CBET 0931988.

#### References

- [1] M. Hu, P. Keblinski, J.S. Wang, N. Ravivakar, Interfacial thermal conductance between silicon and a vertical carbon nanotube, *Journal of Applied Physics* 104 (2008).
- [2] V. Velagapudi, R.K. Konijeti, C.S.K. Aduru, Empirical correlations to predict thermophysical and heat transfer characteristics of nanofluids, *Thermal Science* 12 (2008) 27–37.
- [3] Y. Yang, Z.G. Zhang, E.A. Grulke, W.B. Anderson, G.F. Wu, Heat transfer properties of nanoparticle-in-fluid dispersions (nanofluids) in laminar flow, *International Journal of Heat and Mass Transfer* 48 (2005) 1107–1116.
- [4] G.L. Pollack, Kapitza resistance, *Reviews of Modern Physics* 41 (1969) 48.
- [5] E.T. Swartz, R.O. Pohl, Thermal-Boundary Resistance *Reviews of Modern Physics* 61 (1989) 605–668.
- [6] R.S. Prasher, P.E. Phelan, A scattering-mediated acoustic mismatch model for the prediction of thermal boundary resistance, *Journal of Heat Transfer-Transactions of the ASME* 123 (2001) 105–112.
- [7] A. Maiti, G.D. Mahan, S.T. Pantelides, Dynamical simulations of nonequilibrium processes - heat flow and the Kapitza resistance across grain boundaries, *Solid State Communications* 102 (1997) 517–521.
- [8] J.L. Barrat, F. Chiaruttini, Kapitza resistance at the liquid–solid interface, *Molecular Physics* 101 (2003) 1605–1610.
- [9] D. Chaudhuri, A. Dhar, Heat conduction in a confined solid strip: response to external strain, *Physical Review E* 74 (2006).
- [10] D. Torii, T. Ohara, K. Ishida, Molecular-scale mechanism of thermal resistance at the solid–liquid interfaces: influence of interaction parameters between solid and liquid molecules, *Journal of Heat Transfer-Transactions of the ASME* 132 (2010).
- [11] C. Liu, H.B. Fan, K. Zhang, M.M.F. Yuen, Z.G. Li, Flow dependence of interfacial thermal resistance in nanochannels, *Journal of Chemical Physics* 132 (2010).
- [12] B.H. Kim, A. Beskok, T. Cagin, Thermal interactions in nanoscale fluid flow: molecular dynamics simulations with solid–liquid interfaces, *Microfluidics and Nanofluidics* 5 (2008) 551–559.
- [13] B.H. Kim, A. Beskok, T. Cagin, Molecular dynamics simulations of thermal resistance at the liquid–solid interface, *Journal of Chemical Physics* 129 (2008).
- [14] B.H. Kim, A. Beskok, T. Cagin, Viscous heating in nanoscale shear driven liquid flows, *Microfluidics and Nanofluidics* 9 (2010) 31–40.
- [15] B. FrantzDale, S.J. Plimpton, M.S. Shephard, Software components for parallel multiscale simulation: an example with LAMMPS, *Engineering With Computers* 26 (2010) 205–211.
- [16] J. Mei, J.W. Davenport, G.W. Fernando, Analytical embedded-atom potentials for FCC metals - application to liquid and solid copper, *Physical Review B* 43 (1991) 4653–4658.
- [17] M. Grujicic, G. Cao, W.N. Roy, Computational analysis of the lattice contribution to thermal conductivity of single-walled carbon nanotubes, *Journal of Materials Science* 40 (2005) 1943–1952.
- [18] P.M. Agrawal, B.M. Rice, D.L. Thompson, Predicting trends in rate parameters for self-diffusion on FCC metal surfaces, *Surface Science* 515 (2002) 21–35.
- [19] J.W. Che, T. Cagin, W.A. Goddard, Thermal conductivity of carbon nanotubes, *Nanotechnology* 11 (2000) 65–69.
- [20] X.P. Huang, X.L. Huai, S.Q. Liang, X.W. Wang, Thermal transport in Si/Ge nanocomposites, *Journal of Physics D-Applied Physics* 42 (2009).
- [21] R.J. Stevens, L.V. Zhigilei, P.M. Norris, Effects of temperature and disorder on thermal boundary conductance at solid–solid interfaces: nonequilibrium molecular dynamics simulations, *International Journal of Heat and Mass Transfer* 50 (2007) 3977–3989.
- [22] A.J.H. McGaughey, M. Kaviani, Thermal conductivity decomposition and analysis using molecular dynamics simulations. Part I. Lennard–Jones argon, *International Journal of Heat and Mass Transfer* 47 (2004) 1783–1798.
- [23] H.M. Roder, C.A.N. Decastro, U.V. Mardolcar, The thermal-conductivity of liquid argon for temperatures between 110 K and 140 K with pressures to 70 MPa, *International Journal of Thermophysics* 8 (1987) 521–540.
- [24] L. Xue, P. Keblinski, S.R. Phillpot, S.U.S. Choi, J.A. Eastman, Two regimes of thermal resistance at a liquid–solid interface, *Journal of Chemical Physics* 118 (2003) 337–339.
- [25] P. Borgelt, C. Hoheisel, G. Stell, Exact molecular-dynamics and kinetic-theory results for thermal transport-coefficients of the Lennard–Jones argon fluid in a wide region of states, *Physical Review A* 42 (1990) 789–794.
- [26] B.J. Bailey, K. Kellner, Thermal conductivity of liquid and gaseous argon, *Physica* 39 (1968) 444.
- [27] H. Ziebland, J.T.A. Burton, The thermal conductivity of nitrogen and argon in the liquid and gaseous states, *British Journal of Applied Physics* 9 (1958) 52–59.